



Characterizing pulse reverse-pulse uranium recovery in molten LiCl-KCl with intermittent electrochemical impedance spectroscopy

Jeffrey Eakin^{a,*}, Cornelius Ivory^{a,b}

^a Gene and Linda Voiland School of Chemical Engineering and Bioengineering, Washington State University, Pullman, WA, USA

^b Affiliate Professor, Department of Chemistry, College of Arts and Sciences, Washington State University, Pullman, WA, USA

ARTICLE INFO

Keywords:

Actinide
Uranium
Lanthanum
Electrochemical impedance spectroscopy
Molten salt
LiCl-KCl

ABSTRACT

In this work, EIS was applied to characterize the temporal recovery of uranium from UCl_4 onto a tungsten electrode in molten LiCl-KCl salt between sets of pulse reverse-pulse (PRP) deposition steps. Impedance measurements were fitted to an equivalent circuit (EC) model of the electrode interface using Simplex optimization to calculate the double layer capacitance, charge transfer resistance, Warburg impedance, and CPE-restricted diffusion. Diffusion of uranium towards the electrode surface dominated the surface interactions for the first 80 cycles, followed by a transition to kinetic control for the remaining 520 cycles. A decrease in the Warburg impedance showed depletion of uranium from the bulk melt, which was confirmed to be a 52.5% reduction through ICP-OES. Reduction in the phase from CPE-restricted diffusion suggested the formation of pores in the uranium deposits, which was confirmed through SEM characterization.

1. Introduction

Treatment of spent nuclear fuels in molten salts was first demonstrated during the pilot-scale EBR-II experiments in the 1990 s.[1–3] Spent metal fuel was electrorefined for separation of metallic uranium from fuel cladding materials, fuel waste products, and leftover salt wastes. Uranium was recovered into a product stream while the waste products were isolated and fixed into glass-bonded sodalite ceramic. The separation of actinides from other unwanted fission products in the fuel waste is an integral part of the electrorefining process for recycling unused uranium back into fuel for nuclear reactors.

Exploration of numerous methods to electrochemically recover actinides during their separation from unwanted fission products is ongoing. These methods include exhaustive electrolysis through the continuous deposition of actinides onto inert electrodes,[4–10] solid reactive cathodes,[8,11–17] or liquid cathodes,[18–22] pulsed deposition aimed at reducing the formation of uranium dendrites,[10,23] and galvanic replacement of sacrificial metallic species with uranium.[15,24–26] Any of these methods may contribute to improving or complementing the actinide drawdown process during electrorefining.[27].

An area of interest regarding actinide drawdown is the optimization and characterization of uranium deposition. A plethora of tools exist in

aqueous electrochemistry to probe the deposition characteristics of electroactive species onto solid electrodes, including electrochemical scanning tunneling microscopy (EC-STM),[28–33] electrochemical atomic force microscopy (EC-AFM),[30,33–36] electrochemical quartz crystal microbalance (EQCM),[30,37] and electrochemical impedance spectroscopy (EIS).[38–41] Unfortunately, many of these techniques cannot be applied similarly in molten salt electrolytes due to the very high temperatures and high corrosivity of the salt melts. An exception is EIS, which only requires an existing three- or four-electrode setup with a potentiostat already used for electrochemical measurements in molten salts.

EIS is a surface-sensitive, non-destructive technique used to analyze interfacial phenomena occurring on a surface that is in contact with a liquid electrolyte. A small perturbation is applied to a working electrode around a specific potential or current to measure the complex impedance response from the resulting reduction or oxidation reactions on or near the electrode surface. In molten salts, EIS has been applied to study the redox characteristics of uranium ions on solid electrodes [42–46] and liquid electrodes [46–47] during deposition.

In this work, the impedance of uranium deposition onto a tungsten working electrode was measured with potentiostatic-EIS (P-EIS) between sets of pulse reverse-pulse (PRP) deposition steps. Lanthanum was first deposited onto the working electrode in a very short applied

* Corresponding author.

E-mail address: jeffrey.eakin@wsu.edu (J. Eakin).

<https://doi.org/10.1016/j.rechem.2023.101068>

Received 1 June 2023; Accepted 9 August 2023

Available online 22 August 2023

2211-7156/© 2023 Washington State University.

Published by Elsevier B.V. This is an open access article under the CC BY license

(<http://creativecommons.org/licenses/by/4.0/>).

cathodic pulse, after which it was stripped off and replaced by uranium during a much longer applied anodic pulse. This process was then continuously repeated to deposit additional uranium onto the electrode. PRP was used to avoid the formation of uranium dendrites on the surface, to take advantage of galvanic replacement observed in previous work,^[26] and to avoid the corrosion of deposited uranium already on the electrode surface at potentials that were equal to or more anodic than uranium's oxidation potential. Simplex optimization was utilized to fit impedance data measured from P-EIS to an equivalent circuit (EC) model that was representative of kinetic and diffusive phenomena occurring at the electrode surface during uranium deposition.

2. Experimental

All experiments were performed in a nitrogen-atmosphere glovebox where the oxygen concentration was maintained below 1 ppm. Inside of the glovebox was a Kerr-lab electric melt furnace that had been modified to allow for vertical insertion of electrodes through the top of the lid and for manipulation of the lid while at operating temperature.

An image of the furnace inside of the glovebox is shown in Fig. 1(a). To isolate the electrodes from the metallic components of the furnace lid, 3 mm OD \times 1.5 mm ID quartz tubes were inserted into three 2.9 mm silicone holes at the top of the lid. This configuration allowed for manual manipulation of each electrode during experimentation.

The electrochemical cell consisted of a 36 mm diameter, 43 mm long glassy carbon crucible pictured in Fig. 1(b). The working electrode was a 1 mm diameter tungsten wire that was electrochemically polished by immersing 4 cm of the wire into a 5 wt% NaOH aqueous solution and applying an 8 V potential for 60 s to corrode the outer-most tungsten layer. The counter electrode was a 3 mm diameter \times 15 mm long graphite rod with a 1 mm diameter tungsten wire inserted into a 1 mm hole drilled at the top of the rod. The pseudo-reference electrode was a 1 mm Ag wire immersed within a 10 wt% AgCl-LiCl-KCl melt inside of a graphite sheath. Full details on the preparation of this reference electrode are detailed in previous work.^[26]

Anhydrous LiCl-KCl eutectic (99.99%) and anhydrous LaCl₃ (99.9%) were purchased from Sigma-Aldrich. Details on UCl₄ synthesis are provided in previous work ^[26,48] and was performed by Erik Reinhart

from Dr. James Boncella's research group in the Department of Chemistry in the College of Arts and Sciences from Washington State University. Electrochemical measurements were obtained and experiments were performed using a Gamry Interface 1010E potentiostat.

The molten electrolyte was prepared by mixing 13 g of LiCl-KCl eutectic with 1 wt% LaCl₃ and 0.15 wt% UCl₄ into a solid mixture and heating to 550 °C inside of the furnace. La was chosen as the sacrificial metal for replacement with U during the reverse-pulse step because La represents the different lanthanides that would be present in spent nuclear fuel due to the chemical and electrochemical similarities of the lanthanides. Additionally, previous work has demonstrated that the additional reduction step necessary to reduce UCl₄ to metallic U does not interfere with the recovery process ^[26].

After reaching temperature, the electrodes were lowered into the molten electrolyte to a depth of 12 mm. The electrochemical cell was left to equilibrate for 1 h and confirmed by measuring the open circuit potential over 10 min.

A schematic of how PRP with EIS was performed through Gamry Framework's Sequence Wizard is provided in Fig. 2. The electrode was electrochemically cleaned using chronoamperometry at 0 V for 30 s to strip off any of the cathodic species that may have adhered to the surface. The open circuit potential was then measured for 5 min to perform EIS at 0 V vs OCP and measure the impedance of the bare tungsten wire before PRP. PRP was then run for 20 cycles where each forward pulse was at -2.5 V vs. Ag/AgCl for 30 ms followed by the reverse pulse at -1.7 V vs. Ag/AgCl for 5 s. At the end of the 20th cycle, EIS was run at -1.7 V vs. Ag/AgCl to measure the impedance of uranium deposition onto the tungsten electrode. EIS was applied at -1.7 V vs. Ag/AgCl so that U may continue depositing onto the tungsten electrode at this potential for comparison with U deposition at different times during the deposition process. This chosen potential was also sufficiently cathodic enough to prevent U corrosion on the tungsten electrode.

3. Theory

3.1. Equivalent circuit models

Equivalent circuit (EC) models are circuit diagrams that are

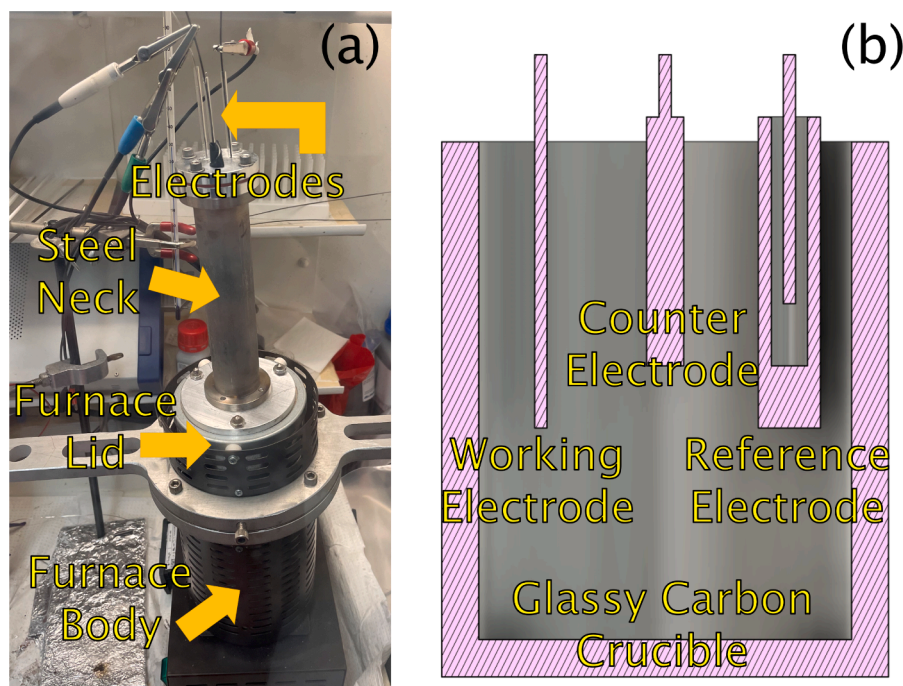


Fig. 1. Pictures of the (a) electric melt furnace and (b) electrochemical cell setup used during experimentation.

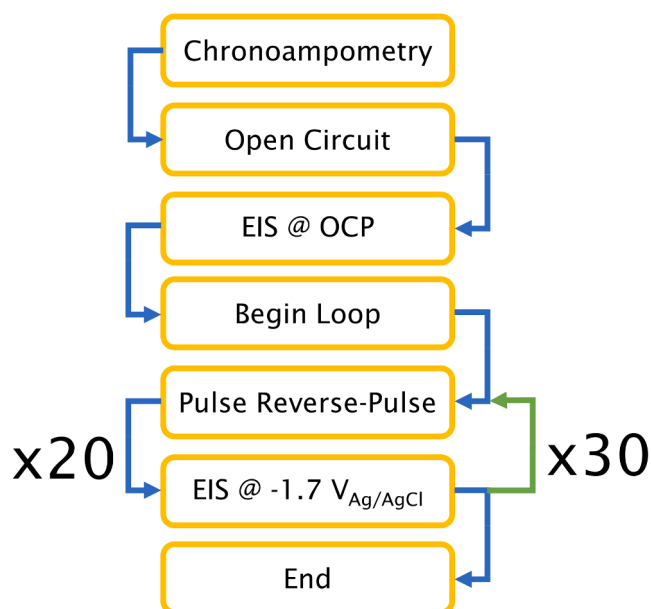


Fig. 2. Flowsheet visualizing the process steps taken during experimentation. Steps were ordered using Gamry Framework's Sequence Wizard to automate the potentiostat electrochemically cleaning the working electrode before switching between depositing uranium with PRP and measuring the impedance during deposition with EIS.

representative of a physical system present at the surface of an electrode. A well-designed EC model was necessary to obtain a good fit with the impedance data from EIS measurements, so it was important to include all of the relevant physical phenomena that may occur at the surface of an electrode during electrodeposition. A good starting model was the modified Randle's Cell EC model shown in Fig. 3. This model includes the uncompensated resistance of the bulk solution between the reference and working electrodes (R_u), the capacitance of the double layer that forms between charged species at the surface of the electrode and counter charges from the bulk solution (DLC), the resistance to charge transfer from electrochemical reactions occurring at the electrode surface (R_{ct}), and the diffusion of charged species towards or away from the electrode surface (Z_w). If additional physical phenomena are known to exist, it may be possible to add more parameters to the EC model to better fit impedance data.

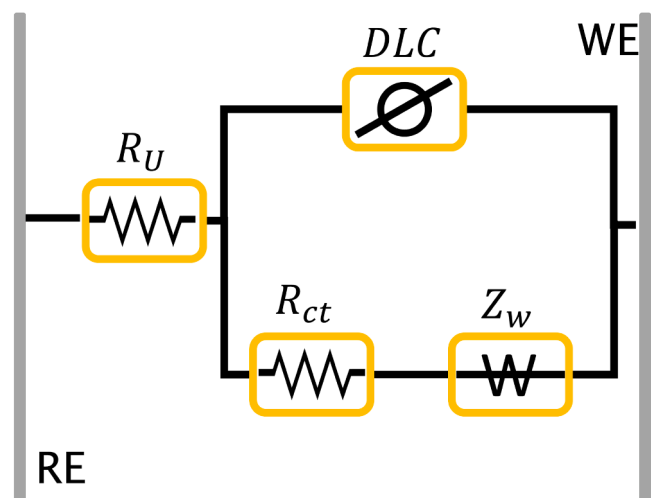


Fig. 3. EC model of a modified Randle's Cell.

3.2. Phasance

A parameter included in Fig. 3 to represent double layer capacitance is what is known as a constant phase element (CPE). CPEs are the circuit elements for inductance, resistance, and capacitance where the phase angle of the sinusoidal wave has been displaced and does not perfectly equal 90° , 0° , and -90° respectively.[49] This displacement is known as phasance. A summary of how inductance, resistance, and capacitance are related to impedance and phasance is provided in Table 1.

Phasance has units of $\Omega \cdot s^a$ where a is a dimensionless characterization of the constant energy efficiency of the CPE given by the equation

$$a = 2\varphi/\pi \quad (1)$$

where φ is the phase angle displacement in radians. $a = -1$ represents a perfect capacitor, 0 a perfect resistor, and 1 a perfect inductor. An example of what this physically means would be the double layer between the surface of an electrode and a bulk electrolyte. For a double layer to behave like a capacitor (-1), the charge distribution on the electrode surface would consist of just positive or negative charges while the bulk interface with the electrode surface would consist of only opposite charges. However, this is not true, including with molten salts, [50–54] where screening of the double layer has charges at the bulk interface with the electrode surface that are imperfectly distributed between negative and positive charges. Therefore, it is useful to think of the CPE for the double layer as an "imperfect capacitor" where a is a dimensionless characterization of that imperfection. Results from Simplex optimization for CPE parameters used an inverted form of phasance shown in Table 1 given by the equation

$$Z = \frac{1}{Y_0(i \cdot \omega)^a} \quad (2)$$

4. Results and discussion

4.1. PRP-EIS

A Bode plot of the EIS impedance spectra from PRP of La with U are presented in Fig. 4. Kramers-Kronig analysis has been provided in Fig. S1 in the supplementary and a Nyquist diagram of the impedance spectra has been provided in Fig. S2. The impedance of the bare tungsten wire at the open circuit potential before starting PRP (pre-PRP) was included for comparison with 100, 200, 300, 400, 500, and 600 PRP cycles. Tungsten is an inert material in LiCl-KCl-LaCl₃-UCl₄ so La and U will not spontaneously adsorb to the electrode surface without the application of an external potential. Therefore, the only two components typically necessary to include in the equivalent circuit model are R_u and DLC, shown in Fig. 5(a). Without adsorption of La or U at the surface, either at open circuit or with an external potential, the only physical phenomena

Table 1
Equations relating inductance, resistance, and capacitance with impedance and phasance.

| Circuit Element | Impedance Relation |
|--------------------|--|
| Inductance (L) | $Z = L \cdot i \cdot \omega$ |
| Resistance (R) | $Z = R$ |
| Capacitance (C) | $Z = \frac{1}{C \cdot i \cdot \omega}$ |
| Phasance (Y_0) | $Z = Y_0(i \cdot \omega)^a$ |

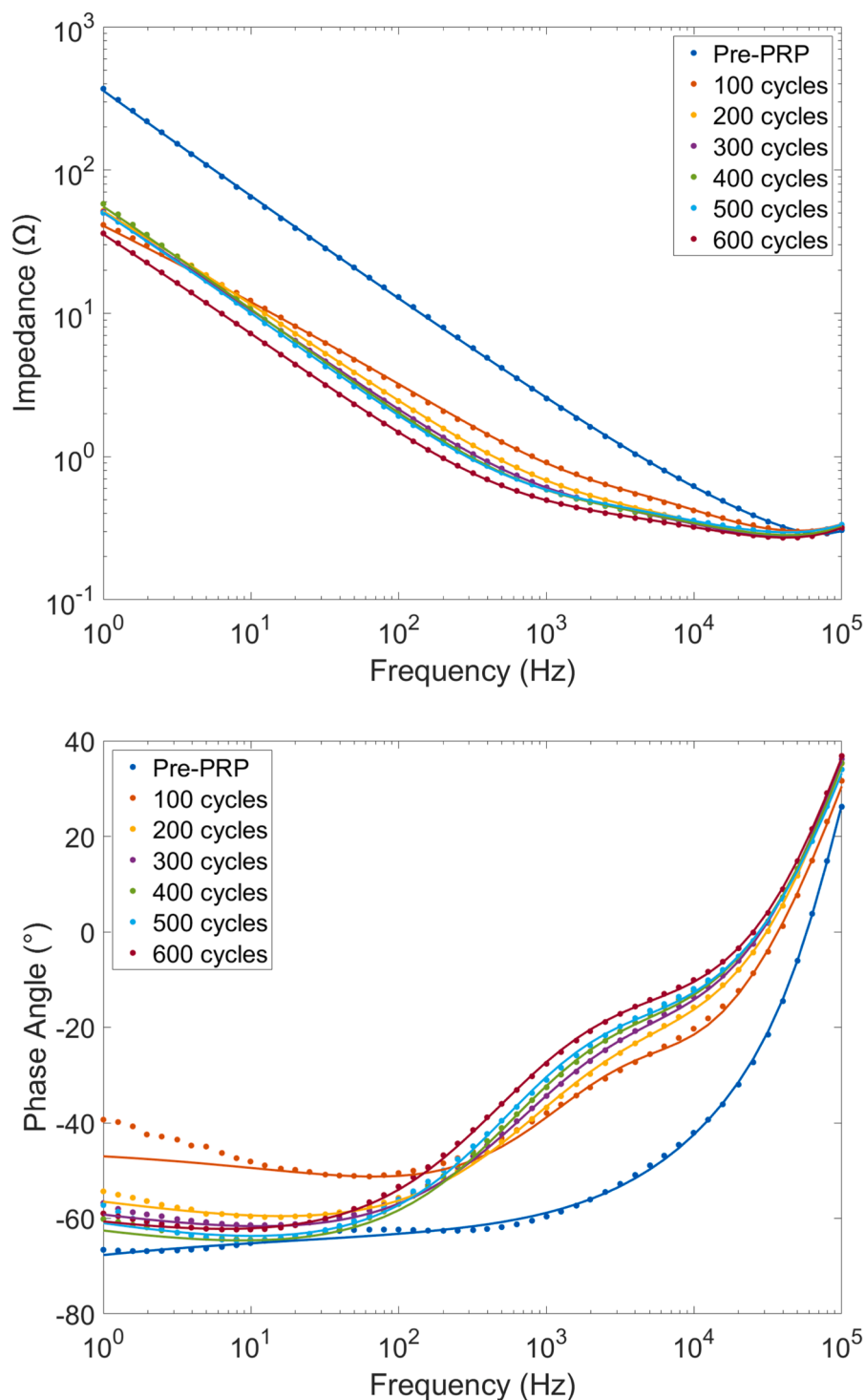


Fig. 4. Bode plots measuring the (a) impedance of deposition of uranium onto the working electrode before PRP and then for every 100 cycles of PRP up to 600 cycles, (b) Kramers-Kronig fit verifying the relationship between the real and imaginary parts of the complex impedance function, and (c) Simplex fitting of the impedance data using the EC model shown later in Fig. 5(b).

that would contribute to the measurable impedance would be the resistance of the bulk molten salt itself and the double layer that forms between the solid surface and liquid interface. However, for consistency during fitting, the EC model in Fig. 5(b) was used to fit the pre-PRP data. This provided a check to ensure that the tungsten wire was clean following the chronoamperometry cleaning step and a control to observe changes to the electrode surface following the first 20 PRP

cycles.

EIS was performed at the end of every 20th PRP cycle. Any surface interactions observed are a result of deposition of U^0 through the reduction reaction



or through reduction of U^{4+} to U^{3+} ions near the electrode surface

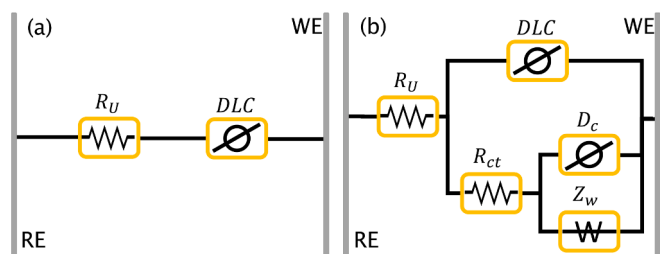


Fig. 5. EC models of (a) the working electrode surface before PRP deposition of uranium and (b) the working electrode surface during deposition of uranium at $-1.7 \text{ V}_{\text{Ag}/\text{AgCl}}$ after every 20 PRP cycles.

through the reaction



Impedance data from every 20th cycle of PRP was fit to the EC model shown in Fig. 5(b) using Simplex optimization. This model retains R_U and DLC but now also includes the kinetic (R_{ct}) and diffusion effects (Z_w and D_c) from equations (3) and (4). The kinetics are dependent on the reaction rate of the two reactions in equations (3) and (4) at the electrode surface while diffusion is broken up into two separate parameters. The Warburg diffusion (Z_w) describes the diffusion of charged species to or from the electrode surface while the CPE-restricted diffusion parameter (D_c) represents impedance contributions from the porosity of the uranium surface deposit that inhibits the diffusion of charge species. [55] The inclusion of D_c in the model assumes that charge transfer at the interface between the deposited uranium and tungsten working electrode is diffusion-limited and dependent on the porosity of the interfacial geometry. The phasance of this CPE represents the porosity of the interfacial geometry such that a phasance close to 0 implies greater porosity of the interface, while a phasance close to 1 implies a smooth

interface. The results from Simplex fitting the EC model in Fig. 5(b) to the impedance data in Fig. 4 for DLC, R_{ct} , Z_w , and D_c are presented in Fig. 6 with error bars calculated using the Maximum Likelihood Estimation method. [56].

In Fig. 6(a), the DLC followed a logarithmic trend where the DLC increased from near zero after the first 20 cycles of PRP up to approximately 0.90 mS/s^{a1} , where $a1$ is the phasance of the DLC. This behavior was expected as it was hypothesized that the DLC increases steadily over time as more uranium is deposited onto the surface of the electrode, increasing the effective electroactive surface area and, by extension, the total surface of the double layer. The phasance does not follow the same trend as the DLC, however. After decreasing from 1 after 200 cycles, the phasance remains stable at around 0.80. This is likely related to the total surface coverage of uranium as there are less and less exposed tungsten sites for uranium to deposit onto.

R_{ct} in Fig. 6(b) showed interesting behavior. Initially starting at around 0.15Ω , the R_{ct} increased to over 0.45Ω by 100 cycles. After the peak, R_{ct} declined over the remaining 500 cycles and never reached a stable value by the end of the experiment. R_{ct} is inversely proportional to the Butler-Volmer equation, which implied that increases to R_{ct} results in a decrease of the kinetic activity at the surface of the electrode.

In Fig. 5(d), Z_w increased to $24.25 \text{ mS/s}^{0.5}$ by 60 PRP cycles as more and more U^{3+} and U^{4+} from the bulk LKE melt accumulated near the electrode, reduced, and then deposited onto the surface. However, by 80 cycles Z_w started to decrease over the next 100 cycles to around $3.58 \text{ mS/s}^{0.5}$ where it remained approximately the same for the remaining 440 cycles. As uranium was depleted from the system, it was expected that the number of uranium ions migrating towards the surface of the electrode will decrease over time until reaching an equilibrium. At this equilibrium it is difficult to increase the number of uranium ions migrating towards the surface without cathodically increasing the applied reverse-pulse potential.

R_{ct} and Z_w are indications of which mechanism was dominating the

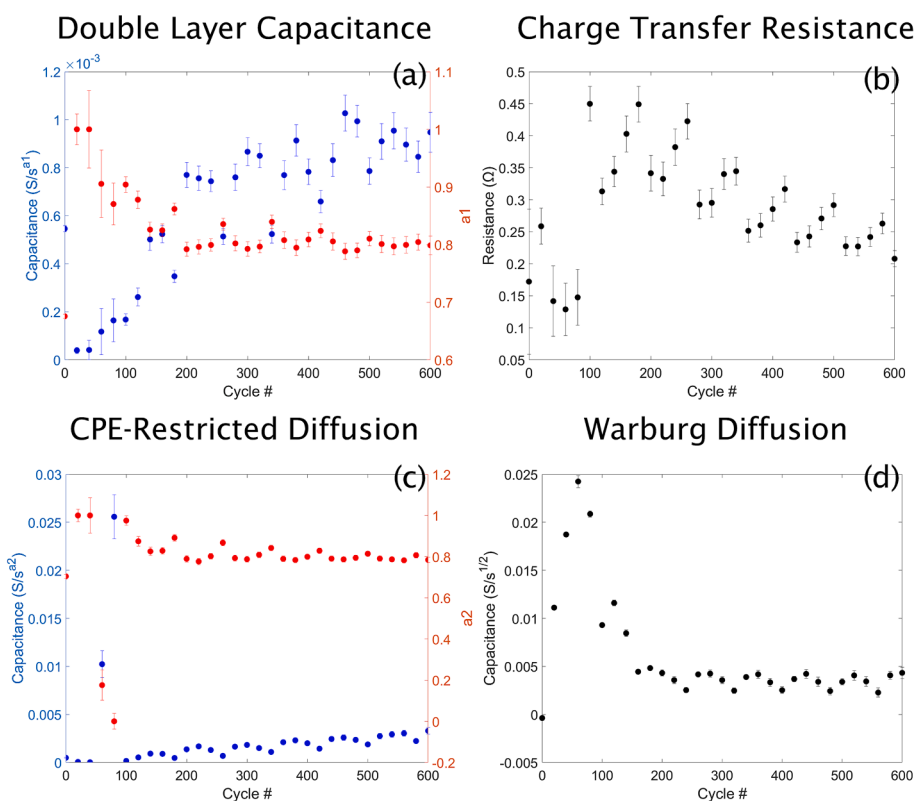


Fig. 6. Results from Simplex fitting measured impedance data for (a) the double layer capacitance, (b) charge transfer resistance, (c) diffusion capacitance, and (d) Warburg diffusion.

impedance response at the surface. Diffusion of charged species towards the electrode controlled the impedance response at the electrode surface for the first 200 cycles, confirming the migration of U ions from the bulk towards the electrode. Following 200 cycles, both Z_w and R_{ct} decreased, showing a transition from diffusion control to kinetic control as the concentration of U ions near the surface increases.

D_c in Fig. 6(c) also showed interesting behavior. For the first 100 PRP cycles, D_c remained around $23.7 \mu\text{S}/\text{s}^{a2}$ with a phasance between 0.9 and 1. D_c then increased linearly over the remaining 500 cycles while the phasance decreased to around 0.8 by cycle 200 and then remained constant for the remaining cycles. The phasance shows a change in the interfacial morphology between the uranium deposit and electrode surface, where the increased roughness contributed to, but did not necessarily correlate with, an increase in the capacitance. The increasing capacitance could be related to the increasing interfacial surface area between the uranium deposit and electrode surface.

4.2. SEM-EDS analysis of the uranium surface deposits

Following uranium deposition using PRP onto the tungsten electrode, samples were imaged using an FEI Apreo VolumeScope SEM. Samples were prepared in the same glovebox as PRP deposition to minimize the total exposure to oxygen and water during transfer from the sealed glass container used to carry samples from the glovebox to the SEM chamber. Upon transfer from the glass container to the SEM

chamber, the samples were exposed to air at 50% humidity for less than two minutes. EDS point analysis was included with SEM imaging using an EDAX Octane Elect EDS system to characterize the atomic composition of the uranium deposits.

During EDS analysis of many sites across different electrode samples it became apparent that there was significant oxidation of all uranium deposits. Slight oxidation of the samples was expected during transfer from the glass container to the SEM chamber, but the extent of oxidation was consistent across all deposit locations. Due to the very dark color of the tungsten electrode after uranium deposition while still in the glovebox, it is hypothesized that uranium is reacting with trace oxygen from the nitrogen atmosphere and trace water or oxygen found in the reagents. This may be occurring either before or during deposition of uranium onto the electrode, with uranium depositing as UO_2 . Oxidation of uranium deposits is discussed further in section 4.3.

Selected images of uranium deposits on the surface of the tungsten electrode are presented in Fig. 7. Many uranium deposit sites of varying shapes and sizes were found on the electrode surfaces although it was not determined what the thicknesses of these deposits were. SEM imaging alone could not provide an adequate quantitative characterization of the deposit topology, but simple observation of uranium deposits across the electrode appeared to be smooth in the SEM images. In addition, deposited uranium formed small rectangular structures varying between $0.5 \mu\text{m} - 1 \mu\text{m}$ in size before coalescing into denser structures. These results are similar to those presented in previously

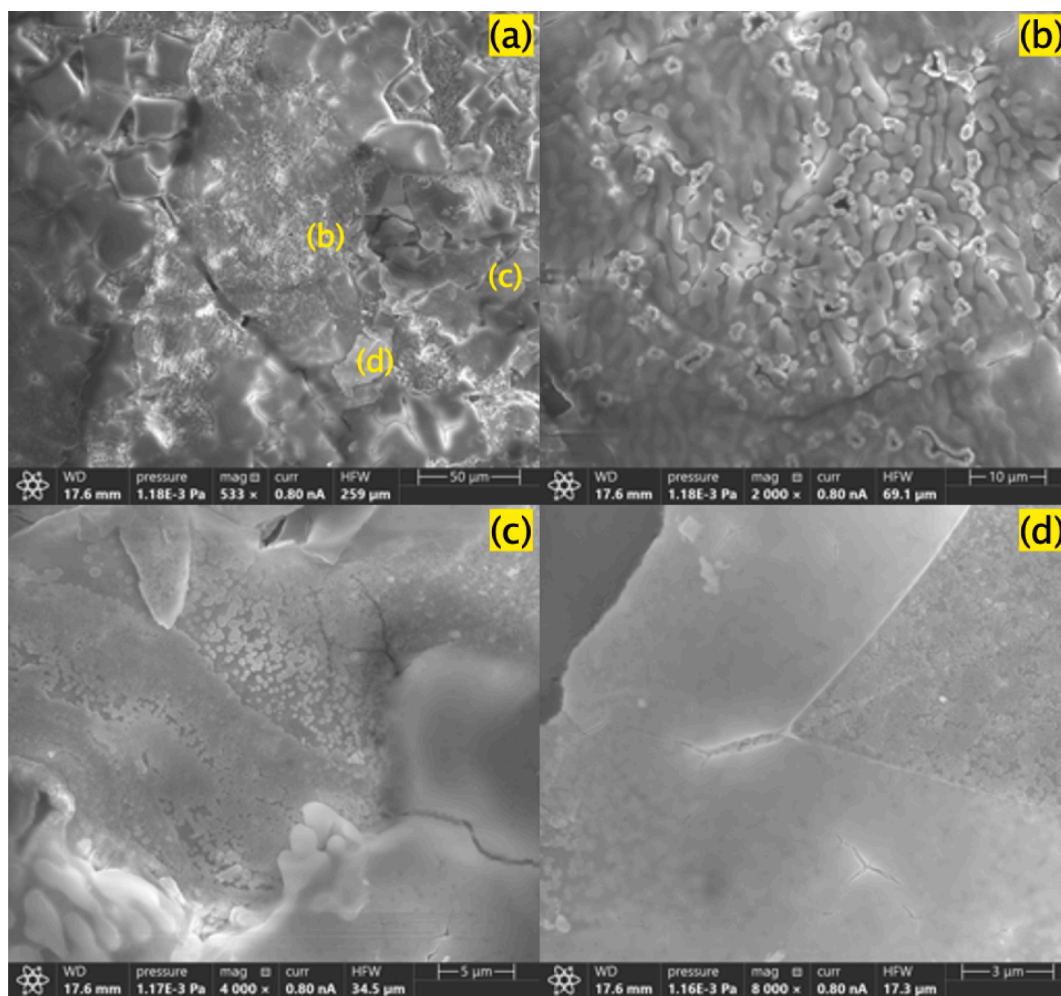


Fig. 7. SEM images taken of (a) a single uranium deposit found on the surface of the electrode after PRP. Areas of (a) were further analyzed in more detail, including elemental analysis with EDS, to characterize the deposit. (b) shows accumulation of highly oxidized uranium agglomerations that are 2 – 5 μm in diameter. (c) and (d) also show different oxidized uranium sites within (a) that were more commonly found across the electrode as well as in previously published work.

published images.[26].

Despite the smooth surface of the uranium deposits, the distribution of uranium across the electrode was not found to be consistent or uniform. Deposits that were within 100 μm of each other were not shaped similarly or connected to each other, creating locations on the surface of the electrode where the total uranium deposition was denser than in other areas. This deposition behavior supports the decrease in the phase angle of D_c where the irregularity of the uranium deposits, even when the deposits are within less than 1 μm of each other, decreases the purely capacitive behavior at the surface. Meanwhile, as these deposits increase in size across the electrode, the capacitance would also increase due to the larger total interfacial area.

4.3. Oxidation of uranium deposits

Fig. 7(b) shows different structures of uranium compared to structures more commonly found across the deposits in Fig. 7(c) and 7(d). EDS analysis of both sites was performed to compare the oxygen atomic percentage and this showed that the uranium deposits in Fig. 7(b) contained more oxygen than the deposits in Fig. 7(c) and 7(d). This may be an indication of UO_2 and UO_{2+x} depositing with distinct structures or different deposition mechanisms.[57] Results are provided in Fig. S3 and S4 in the supplementary information.

Additionally, an orange or rusty-colored substance was frequently observed to be floating on the upper surface of the salt melt after it had cooled and solidified. This substance was determined to be an insoluble, solid UO_2 phase after it was scraped off of the surface of the solidified melt and analyzed using a Panalytical X'Pert PRO diffractometer held in the Institute of Materials Research at Washington State University. Results from PXRD are provided in Fig. S5 in the supplementary.

Previous work has shown that minor contamination of LiCl-KCl-UCl_x melts with oxide ions results in the formation of uranyl species.[58–59] Reagents purchased from Sigma-Aldrich are rated on a trace metals basis so further processing and drying of the reagents before use in experiments may reduce the oxygen available for uranium oxidation. Additionally, the decision to use UCl_4 may be further complicating deposition reactions where U^{4+} could react with dissolved oxygen to form UO_2 . The use of a sacrificial metal such as AlCl_3 to consume oxygen contamination in molten LiCl-KCl may also prevent oxidation of uranium species.[60] AlCl_3 was not used in these experiments to avoid the formation of Al intermetallic compounds with Li, La, and U and due to Al's anodic redox potential compared to U.[61–62].

4.4. Depletion of uranium from the bulk $\text{LiCl-KCl-LaCl}_3\text{-UCl}_4$ melt

The concentration of uranium in the bulk $\text{LiCl-KCl-LaCl}_3\text{-UCl}_4$ following PRP deposition was measured using an Agilent 5100 ICP-OES equipped with an SPS4 autosampler. Samples were prepared by dissolving the 13.11 g chunk of the bulk solidified melt in 500 mL of 2% HNO_3 . After dissolution, five separate samples were made by pipetting 10 mL of the bulk sample solution into 15 mL vials. Calibration curves for lanthanum and uranium were produced by diluting $\frac{1\text{g}}{1\text{L}}$ lanthanum and $\frac{10\text{mg}}{1\text{L}}$ uranium standards purchased from Sigma Aldrich with 2% HNO_3 to obtain linear fits for interpolation or extrapolation of the measured elemental intensity with concentration. Calibration curves are provided in Fig. S6 in the supplementary information.

The concentration of uranium in the 13.11 g bulk melt sample before PRP for comparison after PRP was calculated to be 41.24 mg/L. The concentration of uranium in the bulk melt after PRP was measured to be 20.02 mg/L and the current efficiency of U deposition during both PRP and EIS was calculated to be 40.16%. It was unexpected that so much uranium still remained in the melt after deposition through PRP. However, these results may be biased toward uranium remaining in the bulk melt due to the formation of the UO_2 found floating on top of the melt

after heating.

5. Conclusions

Electrochemical impedance spectroscopy was applied intermittently to measure the impedance of uranium deposition onto the surface of a tungsten electrode between pulse reverse-pulse deposition cycles. Impedance measurements over 600 PRP cycles were fitted using Simplex optimization to equivalent circuit models to calculate the double layer capacitance, charge transfer resistance, Warburg diffusion, and CPE-restricted diffusion. Growth of uranium deposits on the electrode was confirmed due to increases in the double layer capacitance from near zero to 0.90 mS/s^{a1} . Warburg impedance from the diffusion of charged species towards the electrode was observed to peak at around 24.25 $\text{mS/s}^{\text{0.5}}$ by the first 60–80 cycles of PRP. This was followed by a decrease in the Warburg impedance to 3.58 $\text{mS/s}^{\text{0.5}}$ as the kinetics from electrochemical reactions occurring at the electrode surface increased over the remaining 520 cycles. This is represented as a decrease in the charge transfer resistance from 0.45 Ω to 0.25 Ω . The interfacial morphology of the uranium deposits also contributed to the impedance at the electrode surface. Impedance from CPE-restricted diffusion was represented as a constant phase element where the capacitance increased from 23.7 $\mu\text{S/s}^{\text{a2}}$ to 3 mS/s^{a2} while the phase angle decreased from 0.95 to 0.8. SEM imaging of the deposits showed uniformity in the thickness of the deposits, although pores within the deposits themselves may be contributing to the decrease in the phase angle for D_c .

Using EDS, Uranium was found to deposit as an oxidized species rather than as a metal, with this species likely being UO_2 due to the dark color of the electrode after PRP. An insoluble, orange solid phase was also observed to form and float to the surface of the melt after heating and was determined through PXRD to be a separate UO_2 phase. The amount of uranium depleted from the bulk melt was measured to be 52.5% using ICP-OES and the current efficiency of uranium deposition during both PRP and EIS was calculated to be 40.16%.

The severe oxidation of uranium in high-purity molten LiCl-KCl within a nitrogen atmosphere with less than 1 ppm oxygen was unexpected and may prove difficult to overcome in industrial applications if the goal is to recover uranium metal. Further investigation to complement existing literature on the spontaneous formation of oxidized uranium species and their distribution within molten LiCl-KCl is important in order to understand the thermodynamics of these systems. Additionally, it may be worth exploring whether electrochemical reactions during deposition of uranium onto an inert electrode accelerates the formation of these oxidized species.

Declaration of Competing Interest

The authors declare that they have no known competing financial interests or personal relationships that could have appeared to influence the work reported in this paper.

Data availability

Data will be made available on request.

Acknowledgements

This research is supported by the Department of Energy, National Nuclear Science Administration under Award Number DE-NA0003763. Portions of this research were also supported by the Alexandra Navrotsky Institute for Experimental Thermodynamics.

We thank Dr. James Boncella from the Department of Chemistry for providing dehydrated UCl_4 used in all experiments. We also thank Malin Christian Wilkins (Chris) from the Institute of Materials Research at WSU for performing PXRD analysis on samples obtained from experiments. All SEM images were obtained through the Franceschi

Microscopy and Imaging Center at WSU.

Appendix A. Supplementary data

Supplementary data to this article can be found online at <https://doi.org/10.1016/j.rechem.2023.101068>.

References

- [1] R. Benedict, M. Goff, G. Teske, T. Johnson, *J. Nucl. Sci. Technol.* 39 (2002) 749–752.
- [2] M.F. Simpson, K.M. Goff, S.G. Johnson, K.J. Bateman, T.J. Battisti, K.L. Toews, S. M. Frank, T.L. Moschetti, T.P. O'Holleran, W. Sinkler, *Nuclear Technology* 134 (3) (2001) 263–277.
- [3] S.M. McDevitt, D.P. Abraham, J.Y. Park, *Journal of Nuclear Materials* 257 (1) (1998) 21–34.
- [4] S.A. Kuznetsov, H. Hayashi, K. Minato, M. Gaune-Escard, *J. Electrochem. Soc.* 152 (2005) C203.
- [5] P. Souček, R. Malmbeck, C. Nourry, J.P. Glatz, *Energy Procedia* 7 (2011) 396–404.
- [6] P. Souček, R. Malmbeck, E. Mendes, C. Nourry, J.P. Glatz, *J. Radioanal. Nucl. Chem.* 286 (2010) 823–828.
- [7] F. Jiang, W. Huang, H. Zheng, T. Zhu, C. She, S. Gao, D. Long, Y. Gong, Q. Li, *J. Radioanal. Nucl. Chem.* 311 (2017) 1891–1897.
- [8] P. Souček, K. Uruga, T. Murakami, A. Rodrigues, S. Van Winckel, M. Iizuka, J.-P. Glatz, *J. Nucl. Mater.* 526 (2019).
- [9] H. Li, R. Liu, W. Han, W. Wang, Y. Zhang, Y. Sun, M. Zhang, M. Li, *Electrochim. Acta*, 400, 139474 (2021) 10.1016/j.electacta.2021.139474.
- [10] K. Liu, T. Tan, X. Zhou, N. Zheng, Y. Ma, M. Kang, B. Wang, Z. Chai, W. Shi, *J. Nucl. Mater.*, 555, 153110 (2021) 10.1016/j.jnucmat.2021.153110.
- [11] P. Souček, T. Murakami, B. Claux, R. Meier, R. Malmbeck, T. Tsukada, J.P. Glatz, *J. Nucl. Mater.* 459 (2015) 114–121.
- [12] S. Vandarkuzhali, N. Gogoi, S. Ghosh, B. Prabhakara Reddy, K. Nagarajan, *Electrochim. Acta* 59 (2012) 245–255.
- [13] S. Vandarkuzhali, M. Chandra, S. Gosh, N. Samanta, S. Nedumaran, B.P. Reddy, K. Nagarajan, *Electrochim. Acta* 145 (2014) 86–98.
- [14] D.-D. Wang, Y.-L. Liu, S.-L. Jiang, Y.-K. Zhong, W. Han, M. Li, L. Wang, Z.-F. Chai, W.-Q. Shi, *J. Electrochem. Soc.* 170 (2023), 032501.
- [15] D.-D. Wang, Y.-L. Liu, D.-W. Yang, Y.-K. Zhong, W. Han, L. Wang, Z.-F. Chai, W.-Q. Shi, *Sep. Purif. Technol.*, 292, 121025 (2022) 10.1016/j.seppur.2022.121025.
- [16] Y. Liu, K. Liu, L. Luo, L. Yuan, Z. Chai, W. Shi, *Electrochim. Acta*, 275, 100–109 (2018) 10.1016/j.electacta.2018.04.140.
- [17] R. Meier, P. Souček, O. Walter, R. Malmbeck, A. Rodrigues, J.-P. Glatz, T. Fanghanel, *J. Nucl. Mater.* 498 (2018) 213–220.
- [18] V. Smolenski, A. Novoselova, A. Osipenko, M. Kormilitsyn, and Y. Luk'yanova, *Electrochim. Acta*, 133, 354–358 (2014).
- [19] K. Liu, Y.L. Liu, Z.F. Chai, W.Q. Shi, *J. Electrochem. Soc.* 164 (2017) D169–D178.
- [20] S. Seo, S. Choi, B.G. Park, *J. Nucl. Mater.* 491 (2017) 115–125.
- [21] A. Novoselova, V. Smolenski, V. A. Volkovich, A. A. Ryzhov, Y. Yan, Y. Xue, F. Ma, *J. Electroanal. Chem.*, 906, 116012 (2022) 10.1016/j.jelechem.2022.116012.
- [22] G.Y. Kim, C.H. Lee, D. Yoon, J. Jang, S.J. Lee, *Sci. Technol. Nucl. Install.* 2021 (2021) 5788732.
- [23] C.H. Lee, T.-J. Kim, S. Park, S.-J. Lee, S.-W. Paek, D.-H. Ahn, S.-K. Cho, *J. Nucl. Mater.* 488 (2017) 210–214.
- [24] P. Bagri, C. Zhang, and M. F. Simpson, *J. Nucl. Mater.*, 493, 120–123 (2017) 10.1016/j.jnucmat.2017.06.007.
- [25] P. Bagri, J. Ong, C. Zhang, M.F. Simpson, *J. Nucl. Mater.* 505 (2018) 149–158.
- [26] J. Eakin, D. Molina, X. Guo, H. Beyenal, C.F. Ivory, *J. Electrochem. Soc.* 170 (2023), 032504.
- [27] P. Baron, Y.-J. Choi, *Spent Nuclear Fuel Reprocessing Flowsheet* (2012).
- [28] S. Takakusagi, K. Kitamura, K. Uosaki, *J. Phys. Chem. C* 112 (2008) 3073–3077.
- [29] N. Bock, A. De Clercq, L. Seidl, T. Kratky, T. Ma, S. Gunther, U. Kortz, U. Heiz, F. Esch, *ChemElectroChem* 8 (2021) 1280–1288.
- [30] T. Carstens, A. Ispas, N. Borisenko, R. Atkin, A. Bund, F. Endres, *Electrochim. Acta*, 197, 374–387 (2016) 10.1016/j.electacta.2015.07.178.
- [31] Z. Tan, S. Liu, J. Wu, Z. Nan, F. Yang, D. Zhan, J. Ya, B. Mao, *ChemElectroChem* 9 (2022) 1–8.
- [32] A. Reiser, R. Schuster, R. Spolenak, *Nanoscale* 14 (2022) 5579–5588.
- [33] J. Izquierdo, A. Eifert, C. Kranz, and R. M. Souto, *Electrochim. Acta*, 247, 588–599 (2017) 10.1016/j.electacta.2017.07.042.
- [34] S. M. Walker, M. C. Marcano, W. M. Bender, and U. Becker, *Chem. Geol.*, 429, 60–74 (2016) 10.1016/j.chemgeo.2016.02.025.
- [35] X. Shi, J. Yang, W. Wang, Z. Liu, C. Shen, *Materials (Basel)* 16 (2023) 2278.
- [36] M. Kitta, H. Sano, *Langmuir* 33 (2017) 1861–1866.
- [37] S. Ban, *Dent. Mater. J.*, 4, 476–474 (2003).
- [38] H. Li, D. Dzombak, R. Vidic, *Ind. Eng. Chem. Res.* 51 (2012) 2821–2829.
- [39] Y. Liang, F. Gao, L. Wang, and S. Lin, *J. Memb. Sci.*, 619, 118747 (2021) 10.1016/j.memsci.2020.118747.
- [40] C.J. Li, M. Du, *RSC Adv.* 7 (2017) 28819–28825.
- [41] B. Raman, D. M. Hall, S. J. Shulder, M. F. Caravaggio, and S. N. Lvov, *Colloids Surfaces A Physicochem. Eng. Asp.*, 508, 48–56 (2016) 10.1016/j.colsurfa.2016.08.018.
- [42] B.P. Reddy, S. Vandarkuzhali, T. Subramanian, P. Venkatesh, *Electrochim. Acta* 49 (2004) 2471–2478.
- [43] D. Yoon and S. Phongikaroon, *Electrochim. Acta*, 227, 170–179 (2017) 10.1016/j.electacta.2017.01.011.
- [44] L. Swain, G. Pakhui, A. Jain, S. Ghosh, *J. Electroanal. Chem.* 910 (2022), 116125.
- [45] L. Swain, G. Pakhui, A. Jain, and S. Ghosh, *J. Electroanal. Chem.*, 907, 115969 (2022) 10.1016/j.jelechem.2021.115969.
- [46] G. Y. Kim, D. Yoon, S. Paek, S.-H. Kim, T.-J. Kim, D.-H. Ahn, *J. Electroanal. Chem.*, 682, 128–135 (2012) 10.1016/j.jelechem.2012.07.025.
- [47] D.W. Wang, S.L. Jiang, Y.L. Liu, J.Z. Chen, D.D. Wang, Y.P. Zaikov, L. Wang, Z. F. Chai, W.Q. Shi, *Journal of radioanalytical and nuclear chemistry* 332 (2023) 1377–1387, <https://doi.org/10.1007/s10967-023-08782-y>.
- [48] J.L. Kiplinger, D.E. Morris, B.L. Scott, C.J. Burns, *Organometallics* 21 (2002) 5978–5982.
- [49] J. Jacquelin, *Current Topics in Electrochemistry* 4 (1997) 2–13.
- [50] M.Z. Bazant, B.D. Storey, A.A. Kornyshev, *Phys. Rev. Lett.* 106 (2011) 6–9.
- [51] J. Klos, S. Lamperski, *Electrochim. Acta* 337 (2020), 135747.
- [52] M. Han, H. Kim, C. Leal, M. Negrito, J.D. Batteas, R.M. Espinosa-Marzal, *Adv. Mater. Interfaces* 7 (2020) 1–10.
- [53] R. Downing, G.V. Bossa, S. May, *J. Phys. Chem. C* 122 (2018) 28537–28544.
- [54] Z.A.H. Goodwin, G. Feng, A.A. Kornyshev, *Electrochim. Acta* 225 (2017) 190–197.
- [55] J. Bisquert, G. Garcia-Belmonte, P. Bueno, E. Longo, L.O.S. Bulhões, *J. Electroanal. Chem.* 452 (1998) 229–234.
- [56] F.S.G. Richards, *J.R. Stat. Soc. Ser. B* 23 (1961) 469–475.
- [57] J.M. Elorrieta, L.J. Bonales, N. Rodríguez-Villagra, V.G. Baonza, J. Cobos, *Phys. Chem. Chem. Phys.* 18 (2016) 28209–28216.
- [58] S.A. Kuznetsov, H. Hayashi, K. Minato, M. Gaune-Escard, *Electrochemistry* 73 (2005) 630–632.
- [59] S. Choi, S.-E. Bae, T.-H. Park, *J. Electrochem. Soc.* 164 (2017) H5068–H5073.
- [60] N. Samanta, S. Maji, S. Kumar, P. Venkatesh, M. Chandra, A. Jain, *Journal of radioanalytical and nuclear chemistry* 331 (2022) 5881–5892.
- [61] Y. Li, P. Zhao, Y. Dai, M. Yao, H. Gan, W. Hu, *Fusion Eng. Des.*, 103, 8–12 (2016) 10.1016/j.fusengdes.2015.11.053.
- [62] Y.L. Liu, Y.D. Ya, W. Han, M.L. Zhang, L.Y. Yuan, R.S. Lin, G.A. Ye, H. He, Z. F. Chai, W.Q. Shi, *Electrochim. Acta* 114 (2013) 180–188.